ADVANCED ENERGY MATERIALS
www.advenergymat.de

Importance of Superstructure in Stabilizing Oxygen Redox in P3-$Na_{0.67}Li_{0.2}Mn_{0.8}O_2$

*Eun Jeong Kim, Philip A. Maughan, Euan N. Bassey, Raphaële J. Clément, Le Anh Ma, Laurent C. Duda, Divya Sehrawat, Reza Younesi, Neeraj Sharma, Clare P. Grey, and A. Robert Armstrong**

Activation of oxygen redox represents a promising strategy to enhance the energy density of positive electrode materials in both lithium and sodium-ion batteries. However, the large voltage hysteresis associated with oxidation of oxygen anions during the first charge represents a significant challenge. Here, P3-type $Na_{0.67}Li_{0.2}Mn_{0.8}O_2$ is reinvestigated and a ribbon superlattice is identified for the first time in P3-type materials. The ribbon superstructure is maintained over cycling with very minor unit cell volume changes in the bulk while Li ions migrate reversibly between the transition metal and Na layers at the atomic scale. In addition, a range of spectroscopic techniques reveal that a strongly hybridized Mn 3d–O 2p favors ligand-to-metal charge transfer, also described as a reductive coupling mechanism, to stabilize reversible oxygen redox. By preparing materials under three different synthetic conditions, the degree of ordering between Li and Mn is varied. The sample with the maximum cation ordering delivers the largest capacity regardless of the voltage windows applied. These findings highlight the importance of cationic ordering in the transition metal layers, which can be tuned by synthetic control to enhance anionic redox and hence energy density in rechargeable batteries.

1. Introduction

Manganese-based sodium layered oxides, $Na_xM_yMn_{1-y}O_2$ ($0.4 \le x \le 1.0$, $0.05 \le y \le 0.5$, M = Li, Mg, Ti, Fe, Co, Ni, Zn, and mixtures thereof)[1,2] represent a major family of positive electrode materials for sodium-ion batteries (SIBs). They adopt one of the polymorphs O3, P3, and P2, depending on the coordination environment of the Na ions and the number of MnO_2 slabs in the unit cell.[3] The compositional and structural phase spaces available to these materials are vast, which enables properties such as capacity, rate capability, operating voltage, and cyclability to be carefully tuned.[4,5]

In general, substitution of spectator elements, such as Li,[6] Mg,[7,8] and Zn[9] for Mn provides a rigid crystal structure during cycling and suppresses Jahn–Teller distortions, at the expense of Mn-derived capacity. Additionally, these electrochemically inactive dopants enable the activation of oxygen redox by creating nonbonding O 2p states at the top of the valence band upon desodiation, which represents an effective way to raise the energy density of positive electrode materials.[10–16] However, the oxidation of oxygen at high voltages often leads to large voltage hysteresis due to cationic migration from the transition metal layers to the alkali metal layers with concomitant structural

E. J. Kim, P. A. Maughan, A. R. Armstrong
School of Chemistry
University of St Andrews
St Andrews, Fife KY16 9ST, UK
E-mail: ara@st-andrews.ac.uk

E. J. Kim, P. A. Maughan, C. P. Grey, A. R. Armstrong
The Faraday Institution
Quad One
Harwell Science and Innovation Campus
Didcot OX11 0RA, UK

E. J. Kim, R. Younesi, C. P. Grey, A. R. Armstrong
ALISTORE-ERI
Amiens, Cedex 80039, France

The ORCID identification number(s) for the author(s) of this article can be found under https://doi.org/10.1002/aenm.202102325.

© 2021 The Authors. Advanced Energy Materials published by Wiley-VCH GmbH. This is an open access article under the terms of the Creative Commons Attribution License, which permits use, distribution and reproduction in any medium, provided the original work is properly cited.

DOI: 10.1002/aenm.202102325

E. N. Bassey, C. P. Grey
Department of Chemistry
University of Cambridge
Lensfield Road, Cambridge CB2 1EW, UK

R. J. Clément
Materials Department and Materials Research Laboratory
University of California
Santa Barbara, CA 93106, USA

L. A. Ma, R. Younesi
Ångström Advanced Battery Centre
Department of Chemistry Ångström Laboratory
Uppsala University
Uppsala SE-75121, Sweden

L. C. Duda
Department of Physics and Astronomy
Division of Molecular and Condensed Matter Physics
Uppsala University
Uppsala S-75120, Sweden

D. Sehrawat, N. Sharma
School of Chemistry
UNSW Australia
Sydney, New South Wales 2052, Australia

 © 2021 The Authors. Advanced Energy Materials published by Wiley-VCH GmbH

evolution.[14,15,17,18] Recently, it has been reported that the ribbon superstructure of P2-type $Na_{0.6}Li_{0.2}Mn_{0.8}O_2$ is responsible for the suppression of the voltage hysteresis as a result of the absence of in-plane migration of Mn.[12] In contrast, the honeycomb superstructure, shown in the majority of oxygen active compounds adopting P2, P3, and O3 phases, lowers the reduction voltage of oxygen redox due to the changed local coordination around oxygen as a result of in-plane Mn migration.[12]

Negligible voltage hysteresis is observed in $Na_{4/7}[\square_{1/7}Mn_{6/7}]O_2$ (empty square represents vacancies in Mn sites) possessing inherent vacancies with a unique ordering between vacancies and Mn.[19–21] In this material, the presence of transition metal vacancies not only generates the orphaned O 2p states but also maintains the oxygen stacking sequence without irreversible structural change and cationic migration from the transition metal layers to the Na layers.[19–22] It has also been reported that the design of Mn-deficient compounds is an effective way to activate reversible oxygen redox, by moving O 2p-based states nearer the Fermi level, as shown in $Na_{0.653}Mn_{0.929}O_2$.[23]

Transition metal vacancies in P2-[24] and P3-type[25,26] compounds have been shown to trigger oxidation of oxygen anions independent of the identity of the electrochemically inactive M species, while reversible oxygen redox, namely reduction of oxidized O species, is only observed in the P3-type compounds with a characteristic narrow polarization stemming from the vacancies in the transition metal layers. Additionally, the cation vacancies in P2 type materials[24] activate the oxidation of oxygen at relatively lower voltage compared to those in P3 type[25,26] and $Na_{4/7}[\square_{1/7}Mn_{6/7}]O_2$.[19–22] This variation in the reversibility of oxygen redox processes derived from transition metal vacancies indicates that electrochemical properties can be strongly dependent on the oxygen stacking sequences.

Elucidating the links between the structural polytype (P2, P3, O3) together with the nature of any ordering in the transition metal layer of layered SIB cathodes and their chemical and electronic structure evolution during cycling is vital to identifying the key elements needed to stabilize oxidized O species. Recently, Wang et al. reported anion redox behavior with significant voltage hysteresis in O3 $NaMn_{2/3}Li_{1/3}O_2$ exhibiting honeycomb ordering.[27] This means that it is of particular interest to revisit P3-type $Na_{0.67}Li_{0.2}Mn_{0.8}O_2$ in order to correlate the structure with electrochemical behavior and to gain further insight into the charge compensation mechanism using various spectroscopic techniques.

P3-type $Na_{0.67}Li_{0.2}Mn_{0.8}O_2$ was first described by Du et al. and features highly reversible anion redox behavior with a small voltage hysteresis.[10] This compound was further investigated by Rong et al. who observed a short interlayer O–O distance corresponding to a peroxo-like O–O dimer associated with oxidation of oxygen anions by using neutron total scattering.[11] Although Du et al. recognized the presence of a superlattice in this material, the nature of any Mn/Li ordering has not hitherto been determined. Given the importance of any superlattice ordering in dictating the reversibility and voltage hysteresis of the anion redox properties, as exemplified by the behavior of the different P2 structural analogs reported by House et al. and O3 analog reported by Wang et al.,[12,27] we have performed a thorough structural study of P3-type $Na_{0.67}Li_{0.2}Mn_{0.8}O_2$ in order to determine the nature of the Mn/Li ordering and identify the superlattice. We have identified a ribbon superlattice for this material with a similar arrangement in the Mn/Li layers to that found in P2-type $Na_{0.6}Li_{0.2}Mn_{0.8}O_2$, which also displays a small voltage hysteresis.[12] In addition, we have prepared P3-type $Na_{0.67}Li_{0.2}Mn_{0.8}O_2$ under three different synthetic conditions varying the synthesis atmosphere, heat treatment time, and cooling rate to generate different degrees of ordering in the transition metal layers and identify the effect of ordering on the electrochemical properties.[28–30]

All three materials in this study exhibit a high degree of cationic ordering, however the sample with the maximum degree of ordering between Li and Mn exhibits the highest capacity derived from anion redox and improved long-term performance over the voltage window of 1.6–4.4 V. In situ synchrotron diffraction is employed to investigate the structural evolution in the bulk and confirms that the P3 structure is maintained on cycling, with very small volume changes and retention of the superlattice ordering. Solid-state ^{7}Li nuclear magnetic resonance (NMR) spectroscopy is used as a local structural probe to reveal reversible Li^+ ion migration between the transition metal and (vacant) Na layers on charge/discharge. In addition, in-depth studies of electronic structural changes using a range of spectroscopic techniques indicate that strongly hybridized Mn 3d–O 2p orbitals favor ligand-to-metal charge transfer—described as a reductive coupling mechanism—leading to reversible oxygen redox.

2. Results and Discussion

2.1. Characterization of As-Synthetized Materials

PXRD patterns of as-synthesized air–20Li, oxy–20Li and air–20Li–60 h were recorded with Cu Kα_1 radiation (λ = 1.5406 Å). The major diffraction peaks of the PXRD patterns of all samples can be indexed to a simple P3 structural model (space group $R3m$), in which Na^+ ions occupy trigonal prismatic sites in one layer and Li^+ and $Mn^{3+/4+}$ ions are located in octahedral sites in alternate layers in a trigonal unit cell with ABBCCA oxygen stacking. However, the small peaks around 14° and 17–32° are unindexed, along with significant peak broadening/splitting as shown in Figure S1 (Supporting Information). These features originate from a superstructure as indicated by Du et al.,[10] and can be fully indexed on the basis of a lower symmetry triclinic unit cell (space group $P\overline{1}$). Rietveld refinements using a ribbon superstructure model ($a_{super} \approx \sqrt{7}a$, $b_{super} \approx \sqrt{3}a$), where Li^+ ions separate ribbons composed of four Mn ions, as proposed in P2-type $Na_{0.6}Li_{0.2}Mn_{0.8}O_2$,[12] lead to satisfactory fits of the entire patterns with low R-factors (Figure S2, Supporting Information). The Li site was constrained to full occupancy of Li/Mn and the Na and Mn sites were allowed to vary freely. Air–20Li–60 h exhibits the most ordered structure with few antisite defects in the transition metal layers. The refined level of disorder is summarized in Table S1 (Supporting Information). The material was further characterized using synchrotron X-ray diffraction. Atomic displacement parameters for each site type were constrained to be equal (i.e., all Li sites had the same isotropic thermal displacement parameter, which was different from the thermal displacement parameter for Na and

© 2021 The Authors. Advanced Energy Materials published by Wiley-VCH GmbH

Table 1. Rietveld refinement results for synchrotron X-ray diffraction data for as-synthesized air–20Li–60 h (using a superlattice model (space group $P\bar{1}$).

$R_{exp} = 2.82\%$, $R_{wp} = 7.18\%$, $R_p = 5.63\%$

Lattice parameters $a = 7.5392(2)$ Å, $b = 4.9395(2)$ Å, $c = 7.0259(3)$ Å
$\alpha = 118.080(3)°$, $\beta = 102.345(2)°$, $\gamma = 109.111(2)°$, $V = 195.733$ (16) Å^3

Atom	Wyckoff symbol	*x/a*	*y/b*	*z/c*	Occupancy	Biso
Mn1/Li2	2i	0.4001(3)	0.1996(5)	−0.0075(4)	1.000(5)/0	0.12(2)
Mn2/Li3	2i	0.1955(4)	0.5942(7)	−0.0024(4)	0.971/0.029(6)	0.12(2)
Na1	2i	0.6784(10)	0.0298(16)	0.5	0.648(6)	1.58(9)
Na2	2i	0.1955(8)	0.4183(13)	0.4956(7)	0.996(7)	1.58(9)
Li1/Mn3	1a	0	0	0	0.940/0.060(6)	0.1(5)
O1	2i	0.0741(14)	0.808(2)	0.1727(13)	1	0.24(4)
O2	2i	0.6640(11)	0.597(2)	0.1912(12)	1	0.24(4)
O3	2i	0.5364(13)	0.002(2)	0.8493(12)	1	0.24(4)
O4	2i	0.8744(11)	0.232(2)	0.2144(11)	1	0.24(4)
O5	2i	0.7180(12)	0.524(2)	0.8110(14)	1	0.24(4)

so on). Refinement using the ribbon superstructure model, of data collected on an air-20Li-60 h sample gives an excellent fit, with results summarized in **Table 1**. The fitted profile is shown in **Figure 1**, together with a diagram of the superstructure.

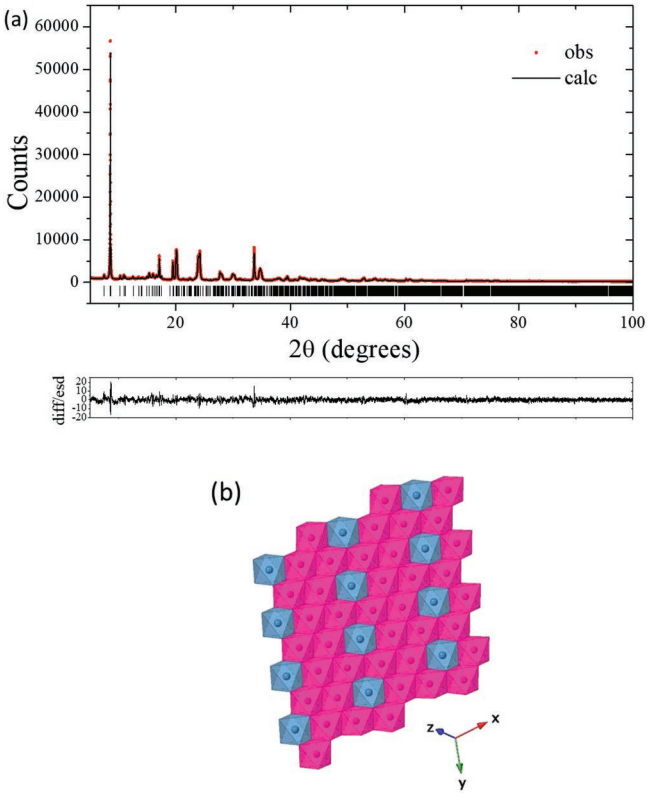

Figure 1. a) Profile fit of synchrotron X-ray diffraction data for as-synthesized air–20Li–60 h using the $P\bar{1}$ space group. Experimental data points are shown in red, with the fitted profile in black and the difference/esd shown below. Tick marks indicate allowed reflections for the $P\bar{1}$ structure. b) Diagram of the superlattice structure used in this study.

Table 2. Ratios of Li resonances obtained by integration of ^{7}Li pj-MATPASS NMR spectra, weighted by the transverse relaxation factor for each site. Note that the % shown here corresponds to the molar % of Li in each of these environments (hence the large value associated with Li_2MnO_3).

	2180 ppm (Li with 6 Mn^{4+} nearest neighbor)	1550 ppm (Li in Mn^{4+} sites in P3 and/or in Li_2MnO_3)	760 ppm (Li_2MnO_3)
Air–20Li	74	8	18
Oxy–20Li	72	9	19
Air–20Li–60 h	90	4	5

Refinement using the ribbon superstructure model of powder neutron diffraction data collected on an air-20Li sample also gives an excellent fit, Figure S3 (Supporting Information), and indicates the presence of 2 wt% of Li_2MnO_3 impurity.

To examine phase purity and the local structure of each sample, we conducted ^{7}Li NMR spectroscopy experiments. As shown in Figure S4 (Supporting Information), all spectra feature three Li resonances at ≈2180, ≈1550, and ≈760 ppm, respectively; the (T_2-weighted) integrals of these isotropic resonances (obtained via pjMATPASS experiments)[31] are given in **Table 2**. Using ab initio calculations of the hyperfine shifts (available from the authors on request), we were able to assign the spectra: the resonance with the highest shift (≈2180 ppm) corresponds to Li nuclei in the transition metal layers surrounded by six nearest-neighbor Mn^{4+}, while the resonance at ≈1550 ppm corresponds to Li nuclei residing in Mn^{4+} sites in the transition metal layers. The latter could be result from antisite disorder in the P3 structure, and/or indicate the presence of an Li_2MnO_3 impurity in the samples. Further evidence for the presence of a small amount of Li_2MnO_3 impurity[32] is provided by the resonance with the lowest shift (≈760 ppm), characteristic of Li in the Li layers in this phase and confirming the observation from powder neutron diffraction.[33,34] ^{7}Li NMR is a particularly sensitive probe of Li_2MnO_3 and of cation ordering in the P3 phase, and integration of the different Li peaks clearly reveals a maximum cationic ordering (≈3% Mn/Li exchange) and a negligible impurity phase in air–20 Li–60 h. Air-20Li and oxy–20 Li exhibit comparable levels of Mn/Li ordering and similar concentrations of Li^+ ions in Li_2MnO_3-like environments. This is in reasonable agreement with the values obtained from X-ray diffraction. Based on these bulk and local structural analyses, it is apparent that a longer heating time favors cationic ordering and suppresses the formation of Li_2MnO_3.

The morphology of the as-synthesized samples was characterized by SEM. The different sintering atmospheres (air vs oxygen) and cooling rate (quench vs 5 °C min^{-1}) have a negligible influence on the morphology for air–20Li and oxy–20Li which exhibit agglomerated primary particles of around 100 nm. However, longer heat treatment time (60 h) tends to enlarge particle size as observed in air–20Li–60 h (**Figure 2**).

2.2. Electrochemical Properties

Electrodes prepared with the air–20Li, oxy–20Li, and air–20Li–60 h samples were cycled over the voltage window 1.6–4.4 V at a rate of 10 mA g^{-1}. As shown in **Figure 3**a, air–20Li–60 h and oxy–20Li deliver comparable initial discharge

© 2021 The Authors. Advanced Energy Materials published by Wiley-VCH GmbH

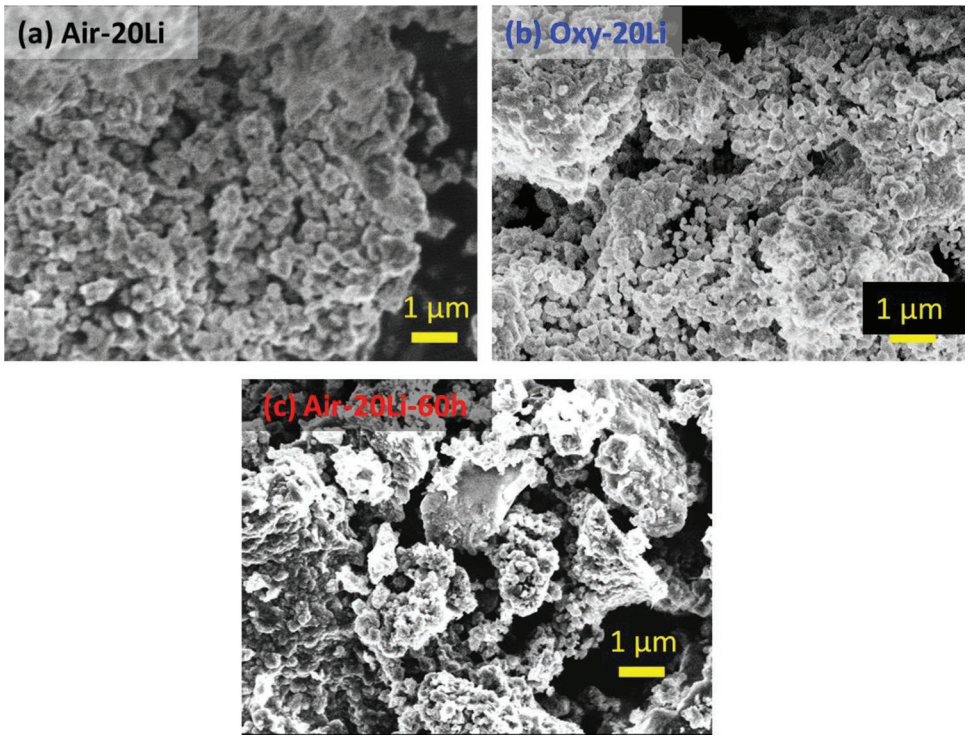

Figure 2. SEM images of as-synthesized. a) Air–20Li, b) oxy–20Li, and c) air–20Li–60 h.

capacities (193 and 191 mAh g^{-1}, respectively) while air–20Li delivers a slightly lower initial capacity of 175 mAh g^{-1}. The low initial capacity of air–20Li is probably due to the somewhat higher concentration of anti-site defects in this material, which we anticipate result in slower Na^+ ion extraction and kinetics. In the case of oxy–20Li, slightly higher cation mixing

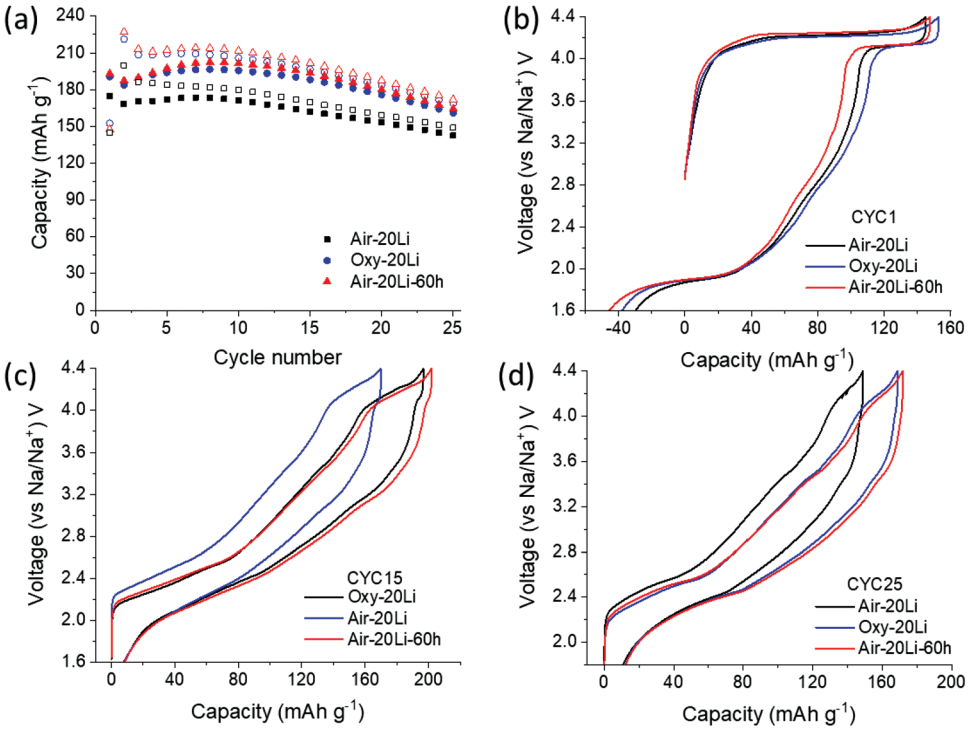

Figure 3. a) Galvanostatic cycling performance of air–20Li (black), oxy–20Li (blue), and air–20Li–60 h (red) cycled at 30 °C in the voltage range 1.6–4.4 V at a rate of 10 mA g^{-1}. Empty and full symbols represent charge and discharge capacity, respectively. Charge/discharge curves of air–20Li (black), oxy–20Li, (blue) and air–20Li–60 h (red) at b) the first cycle, c) cycle 15 and d) cycle 25.

© 2021 The Authors. Advanced Energy Materials published by Wiley-VCH GmbH

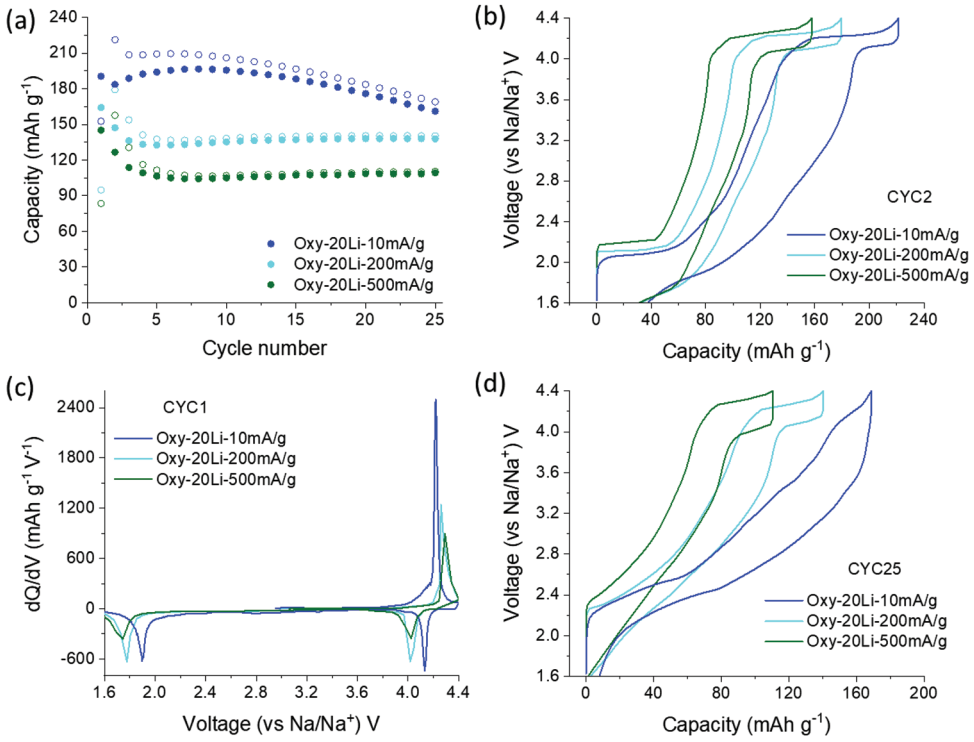

Figure 4. a) Galvanostatic cycling performance of oxy–20Li cycled at 30 °C in the voltage range 1.6–4.4 V at a rate of 10 (blue), 200 (cyan) and 500 (green) mA g^{-1}. Empty and full symbols represent charge and discharge capacity, respectively. Charge/discharge curves at b) the second cycle and d) cycle 25. c) dQ/dV plots for cycle 1.

than air–20Li–60 h, combined with the presence of Li_2MnO_3, cause lower capacity (Figure 3b). Electrochemical profiles for the first charge/discharge cycle (Figure 3b) feature a long plateau on charge, which is partially reversible on discharge, and a narrow polarization of about 0.1 V. The reversible process in the high voltage region for Li-doped sodium manganese oxides ($Na_xLi_yMn_{1-y}O_2$, $x \leq 0.72$, $y \leq 0.24$) adopting either a P3 or P2 structure has been assigned to oxygen redox activated by oxygen anions in Li–O–Na local configurations, proven by various spectroscopic techniques and in-depth structural investigation.[11–12,35] A recent study of P2 layered cathodes by House et al.[12] showed that cation ordering in the transition metal layers dictates the ability of the material to stabilize oxidized O species. In particular, a ribbon-type ordering is reported to inhibit in-plane Mn migration and the consequent formation of molecular O_2 trapped in the transition metal planes. As a result of the stable coordination environment of the oxygen anions, the large voltage hysteresis during discharge observed in most oxygen redox-active compounds is suppressed.[12] Given that the three samples in the current study (air–20Li, oxy–20Li, and air–20Li–60 h) all exhibit a ribbon superlattice structure, the lack of voltage hysteresis is attributed to the nature of the Li–Mn ordering in these compounds. It is worth noting that the longer charge plateau, as compared to the discharge plateau, is primarily a result of electrolyte decomposition for all three materials. This is confirmed by the presence of decomposed electrolyte products in the O 1s XPS spectra, where the concentration of components from C=O and O=C–O increases after charge to 4.4 V and subsequent discharge to 4.1 V (Figure S5, Supporting Information). For all the samples studied here, oxygen redox activity persists for several cycles, as shown in the load curves at cycle 15 (Figure 3c). After 25 cycles at 10 mA g^{-1}, reversible oxygen redox activity is no longer apparent (Figure 3d). This evolution is accompanied by a progressive increase in the voltage associated with $Mn^{3+/4+}$ redox (Figure S6, Supporting Information), in contrast to the gradual voltage decay observed in Li-rich Mn-rich layered compounds in lithium-ion batteries.[36]

Assuming that reduced electrolyte decomposition is likely to enhance the reversibility of oxygen redox, additional cells for oxy–20Li were cycled at rates of 200 and 500 mA g^{-1}. At the faster rates, capacity drops over the first few cycles but stabilizes after 25 cycles (**Figure 4**a). The initial fade is probably due to the increased polarization as shown in Figure 4c. Rate-dependent irreversible reactions in the high voltage region are clearly mitigated at the faster cycling regimes, namely about 53% of charge capacity is reversibly delivered during discharge between 4.0 and 4.4 V at 200 and 500 mA g^{-1} whereas only 33% of charge capacity is reversible at 10 mA g^{-1} on the second cycle (Figure 4b), leading to sustained oxygen redox even at 25 cycles (Figure 4d).

To investigate the effects of structural ordering on the capacity delivered predominantly by oxygen redox, while simultaneously attenuating electrolyte decomposition, all samples were cycled in the narrower voltage window of 3.5–4.3 V at a rate of 10 mA g^{-1}. The highest initial capacity is delivered for the more ordered structure (**Figure 5**a) consistent with the results observed in the wider voltage window. The reversibility

© 2021 The Authors. Advanced Energy Materials published by Wiley-VCH GmbH

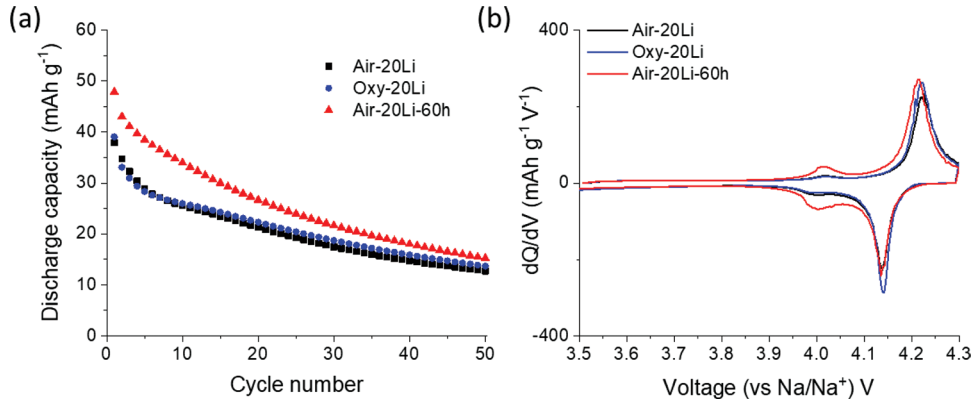

Figure 5. a) Galvanostatic cycling performance of air–20Li (black), oxy–20Li (blue), and air–20Li–60 h (red), cycled at 30 °C in the voltage range 3.5–4.3 V at a rate of 10 mA g^{-1}. b) dQ/dV plots of air–20Li (black), oxy–20Li (blue), and air–20Li–60 h (red) at cycle 25.

of oxygen redox for all samples is notably enhanced as shown at cycle 25 (Figure 5b) compared to that observed at low rates (Figure 3d), probably due to curtailed detrimental reactions on the surface with the electrolyte and reduced lattice stress induced in the low voltage region.

2.3. Structural Evolution in Bulk

Having established the pristine structures and electrochemical behavior of each material, the structural changes during cycling were investigated using in situ synchrotron XRD using air–20Li as a representative material. Selected XRD patterns for as-prepared air–20Li are shown in Figure S7 (Supporting Information) and correspond to samples at the end of the first charge to 4.4 V, at the end of the first discharge to 1.8 V and at the end of the second charge to 4.4 V. The enlarged contour profile map highlights the evolution of the (10$\bar{1}$) and (001) reflections and indicates that the compound exhibits solid solution behavior without evidence for the appearance of new phases during the first two cycles (**Figure 6**a). This is in contrast to the P2-type analog which exhibits a P2 to O2 phase transformation in the high voltage region.[12] Sequential Rietveld refinements were performed on XRD patterns acquired during the first cycle and the second charge to determine how the lattice parameters of the triclinic unit cell evolve. The background was manually fitted and reflections arising from the Al current collector and from the Na metal counter electrode were excluded. The evolution of the unit cell volume and parameters obtained from the sequential Rietveld refinements using the ribbon superlattice model (space group $P\bar{1}$) are overlaid onto the galvanostatic cycling curves in Figure 6b and Figure S8 (Supporting Information), respectively. During the first charge at a rate of 60 mA g^{-1}, the decrease in the unit cell volume is negligible (about 0.15%), although Na^+ ions (0.35 per formula unit) are continuously deintercalated from the structure. On the first discharge and second charge at a slower rate (30 mA g^{-1}), the total volume change between the phases at the end of charge (4.4 V) and end of discharge (1.8 V) is around 0.15%; these processes correspond to the intercalation of 0.3 Na^+ ions and subsequent removal of 0.45 Na^+ ions. Even though the amount of sodium

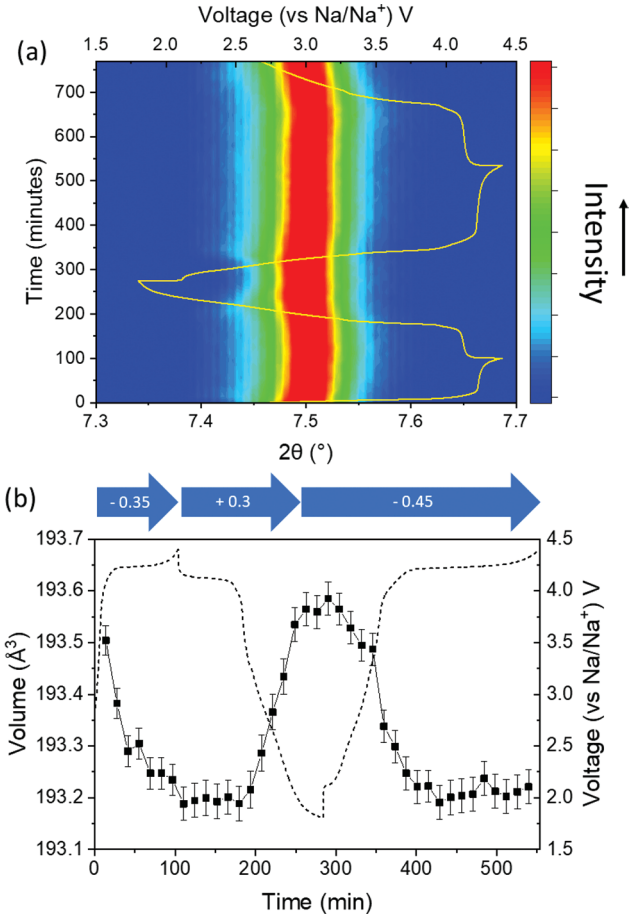

Figure 6. a) Contour plot of in situ synchrotron XRD data collected on air–20Li during the first two cycles. An enlarged 2θ region is shown, highlighting the evolution of the (10$\bar{1}$) and (001) reflections with arbitrary intensity represented using the color scale to the right. Charge/discharge profiles are shown in yellow. b) Evolution of the unit cell volume obtained from sequential Rietveld refinements on XRD patterns acquired during the first cycle and the second charge using the ribbon superlattice model (space group $P\bar{1}$). These data are overlaid with the galvanostatic cycling curves. Arrows indicate the amount of (de)intercalated Na ions in blue.

© 2021 The Authors. Advanced Energy Materials published by Wiley-VCH GmbH

exchanged in the in situ experiment is less than in the galvanostatic cycling compared with other layered SIB cathodes, these strain/volume changes are negligible.[37] The largest strain changes appear to coincide with the $Mn^{3+/4+}$ redox potentials—probably due to Jahn-Teller distortions—while very small changes to volumetric strain occur during the high-voltage charge plateau. The well-maintained superstructure in the least ordered air–20Li material leads unambiguously to the conclusion that the ribbon superstructure will be retained in oxy–20Li and air–20Li–60 h with a higher degree of ordering.

2.4. Local Structural Evolution

While in situ XRD probes long-range structural changes, solid-state NMR gives insight into the local structure evolution during cycling. The ^{7}Li pj-MATPASS spectra of air–20Li at different states of charge are shown in **Figure 7** and Figure S9a (Supporting Information). As mentioned earlier, pristine $Na_{0.67}Li_{0.2}Mn_{0.8}O_2$ features three distinct resonances at approximately 2180 ppm, 1550 ppm, and 760 ppm (labeled A, B, and D, respectively). Our bond pathway analysis reveals that these represent: Li^+ in the transition metal layer surrounded by six Mn^{4+} nearest neighbors; Li^+ in the transition metal layer with four Mn^{4+} nearest neighbors (i.e., Li^+ in the Mn^{4+} positions in the transition metal layer of the P3 structure and/or of an impurity Li_2MnO_3 phase); and Li^+ in the O-type Li layers of an Li_2MnO_3 impurity phase,[32] respectively.

On cycling $Na_{0.67}Li_{0.2}Mn_{0.8}O_2$, the Li_2MnO_3-like feature at 760 ppm remains essentially unchanged in shift or intensity, suggesting that this phase is electrochemically inactive. This is anticipated, as Li^+ is removed from Li_2MnO_3 at higher voltages than those used when cycling $Na_{0.67}Li_{0.2}Mn_{0.8}O_2$. The resonance at 2180 ppm is also present throughout charge and discharge but decreases in intensity at the end of the first and second charge processes and then increases again on discharge, suggesting that Li^+ is removed from the transition metal layers at high voltages, but that the local structure of these Li^+ environments hardly change during Na^+ extraction. The peak at 1550 ppm also decreases in intensity at the end of the first and second charge, by approximately the same amount that the resonance at 2180 ppm decreases, suggesting there is no preferential Li^+ extraction from the two different Li environments in the transition metal layers of the P3 phase (it is assumed that no Li^+ ions are extracted from the Li_2MnO_3 domains).

At the same time as the decrease in intensity of the 2180 ppm feature, a new feature at approximately 450 ppm (labeled E) appears. We assign this feature to Li^+ ions in the Na^+ layer; since the occupation of prismatic sites by Li^+ ions is unfavorable in oxides, we anticipate that Li^+ resides in O-type Na layers generated by local transition metal layer glides within the P3 structure ex situ, since there is no evidence for the large scale formation of O layers in the bulk (according to in situ XRD). These local glides may be induced on resting the cells after cycling, suggesting that migration is thermodynamically favorable but kinetically bypassed during cycling.

The 450 ppm resonance is retained on discharge to 4.1 V but is no longer present in the 1.6 V discharged sample. While this result may indicate that the partial P3–O3 transformation observed in the ex situ 4.4 V charge and 4.1 V discharge samples is fully reversible on discharge, it may also be additional evidence for the fact that the partial O3–P3 transformation is kinetically hindered in situ and is therefore not observed in the 1.6 V sample that has undergone an uninterrupted charge–discharge process. In addition, a new feature at approximately 1250 ppm develops (labeled C), whilst the feature at 2180 ppm decreases in intensity. We assign the 1250 ppm resonance to Li^+ ions occupying transition metal sites with three Mn^{4+} nearest neighbors or to Li^+ nearby Mn^{3+} centers.

At the end of the second charge, the features at 2180, 1550, and 1250 ppm (i.e., Li^+ in the transition metal layer) decrease in intensity or disappear, while the feature at 450 ppm reappears. These low-shift features are also slightly broader than at the end of the first charge, suggesting a wider distribution of Li^+ environments in the O-type Na layers after two charge processes, stimulated by local changes in the bond angles and lengths.

The spectrum on the second discharge to 4.1 V is similar to that obtained on the first discharge to 4.1 V, suggesting that the phases formed on the first and second discharge are similar, as anticipated from the voltage profiles.

Li site occupancies were further monitored by integration of the ^{7}Li pj-MATPASS spectra. Contributions from individual Li sites were scaled by a transverse relaxation factor accounting for the loss of NMR signal intensity over the signal acquisition time. The Li content in the five sites is shown in **Table 3**. The fraction of Li ions in the transition metal layers unambiguously decreases during the first charge, with only 32% Li left in the transition metal layer at the top of charge (CH 4.4 V). After full discharge, the majority of the Li ions return to the original site in the transition metal layers. This largely reversible Li migration is also confirmed on the second cycle. It is expected that the reversibility of Li migration will be enhanced for oxy–20Li and air–20Li–60 h due to their more ordered structure. Based on our ^{7}Li NMR integrals, we see a loss of approximately 20% of signal over the first cycle (compared to the pristine material). Beyond this, little loss occurs on subsequent cycles. The stability on subsequent cycles is likely a densification or reconstruction at the surface, as well as a build-up of a cathode–electrolyte interphase, so that further Li^+ loss is avoided. This observation is consistent with the Li^+ loss observed in P2–$Na_{0.8}[Li_{0.12}Ni_{0.22}Mn_{0.66}]O_2$.[38] In this case, some

Table 3. Distribution of Li sites obtained by integration of ^{7}Li pj-MATPASS NMR spectra.

	A	B	C	D	E
	TM layer	TM layer	TM layer	Li_2MnO_3	Na layer
Pristine	74	8	0	18	0
CH 4.1 V	77	6	0	18	0
CH 4.22 V	65	8	0	19	8
CH 4.4 V	28	4	0	14	54
DIS 4.1 V	51	6	0	17	26
DIS 1.6 V	23	11	37	30	0
Second CH 4.4 V	23	5	0	30	42
Second DIS 4.1 V	56	6	0	20	18

© 2021 The Authors. Advanced Energy Materials published by Wiley-VCH GmbH

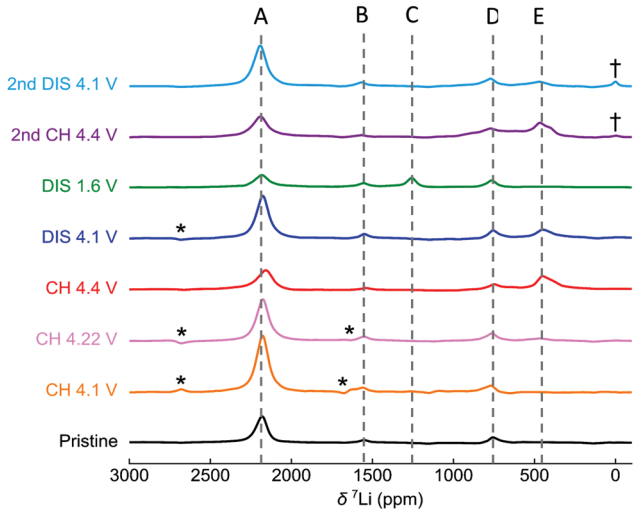

Figure 7. ^{7}Li pj-MATPASS NMR spectra acquired at 4.7 T under 40 kHz magic angle spinning (MAS) on as-prepared material and different stages along with the first and second electrochemical cycles of air–20 Li. * indicates residual sideband, † diamagnetic impurity.

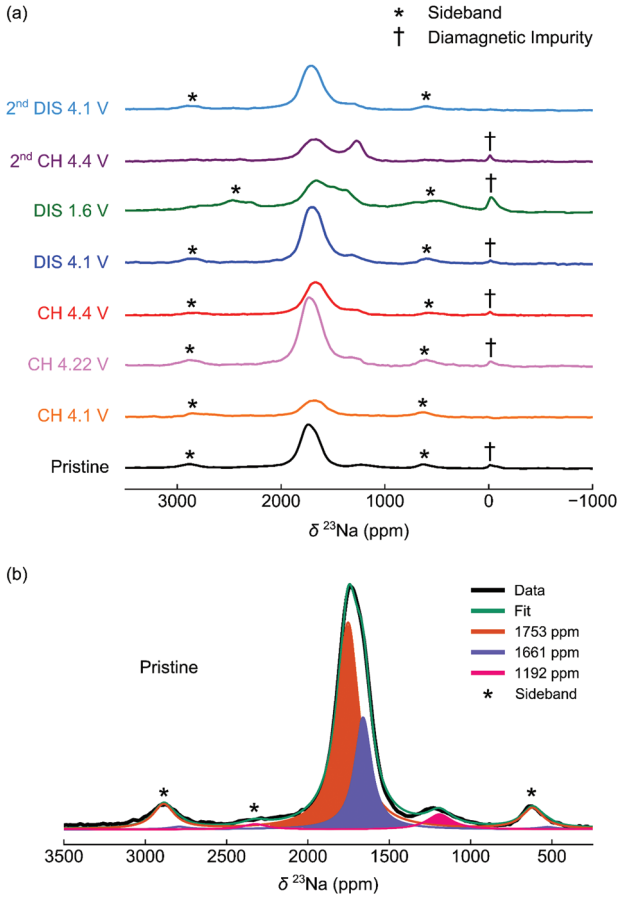

Figure 8. Hahn-echo ^{23}Na NMR spectra for $Na_xLi_{0.2}Mn_{0.8}O_2$, recorded at 4.7 T under 60 kHz magic angle spinning speed. a) The spectra for $Na_xLi_{0.2}Mn_{0.8}O_2$ at different states of charge; all spectra are normalized relative to the number of scans and sample mass. b) A fit to the pristine material spectrum.

Li loss was observed during the first cycle but remained stable on subsequent cycles.

The ^{23}Na Hahn-echo NMR spectra for air–20Li at different states of charge are shown in **Figure 8**a. The pristine material displays three distinct resonances at 1750, 1660, and 1190 ppm, with relative T_2-weighted integral ratios of 11:4:1 (Figure 8b). These integrals indicate that the three resonances do not arise from the three distinct crystallographic Na sites in $Na_{0.67}Li_{0.2}Mn_{0.8}O_2$. Our calculated shifts also do not match the shifts of the features seen, despite the same set of calculations accurately describing the ^{7}Li NMR shifts (see Supporting Information). We therefore attribute the three spectral features to average signals resulting from Na^+ ions hopping between different Na sites (i.e., different Na local environments) associated with different resonant (Larmor) frequencies. In this situation, the signals corresponding to individual sites involved in the Na^+ diffusion process are first broadened and eventually coalesce at high Na^+ chemical exchange rates.[39] The intensities and full widths at half maximum (FWHMs) of the resulting average signals are strongly dependent on the rate of Na^+ hopping. If hopping is fast on the NMR timescale, that is, if the frequency of Na^+ ion hops is much greater than the frequency difference (in Hz) between the signals associated with the exchanging Na sites, Na^+ ions are in the "fast motion" regime and a sharp feature at the thermodynamic average of the Larmor frequency of each site is observed (this average accounts for the relative populations). If hopping is slow on the NMR timescale, Na^+ ions are in the "slow motion" regime and distinct resonances are observed at the characteristic resonant frequencies of the exchanging sites. In the "intermediate" motional regime, (a) broad, low-intensity resonance(s) is(are) observed due to additional T_2 relaxation effects.

Therefore, we anticipate that the sharp features at 1750 and 1660 ppm correspond to "fast-moving" Na^+ (i.e., Na^+ exchanging between sites connected via low activation energy barriers), whilst the 1190 ppm resonance corresponds to "slow-moving" Na^+ (i.e., Na^+ exchanging between sites connected via high hopping barriers). Since we expect rather similar hopping barriers for Na^+ ions occupying a single P3 layer, we assign the "slow-moving" Na^+ to ions trapped in O-type layers (i.e., stacking fault layers).

On charging air–20Li up to 4.1 V, a large decrease in signal intensity is seen for the slow- and fast-moving Na^+ features. We attribute this to overall slower (more infrequent) Na^+ motion, i.e., the "fast-moving" Na^+ ions move into the intermediate regime, whilst the "slow-moving" Na^+ ions move further towards the slow regime, which is also reflected in the evolution of the T_2 relaxation times (Table S2, Supporting Information). This lower mobility may result from Na^+/vacancy charge ordering. The decrease in the observed resonant frequencies at this state of charge is attributed to a change in Na site energies, as expected from a Na^+/vacancy ordered structure (giving rise to different Na site populations and therefore different exchange-averaged shifts as compared to the pristine compound).

Further charging to 4.22 V results in an increase in peak intensity for both the fast- and slow-moving Na^+ features, suggesting faster overall Na^+ ion motion, probably due to an increase in the concentration of vacancies in the structure.

© 2021 The Authors. Advanced Energy Materials published by Wiley-VCH GmbH

Compared to the pristine material, the Larmor frequencies of the sharp features decrease, whilst the Larmor frequency of the broad, low-intensity feature increases. The gradual changes in the observed average resonant frequencies on charge probably reflect both the gradual change in the electronic structure of $Na_xLi_{0.2}Mn_{0.8}O_2$, as well as changes in Na site populations. No new features appear in the ^{23}Na NMR spectra at the end of the first charge, despite the local formation of O-type layers ex situ, as observed with ^{7}Li NMR. This suggests that Na^+ does not occupy the O-type layers as they form—, i.e., Na^+ ions only occupy the P-type layers in the structure.

On initial discharge to 4.1 V, the resonances remain almost unchanged compared to those observed at the top of charge, apart from a slight broadening of the fast-moving Na^+ resonance, suggesting a greater distribution of Na^+ sites than on charge; this is consistent with the ^{7}Li NMR, where local environmental disorder was observed.

At the end of the first discharge, several overlapping resonances appear at approximately 1460 ppm (between the fast- and slow-moving Na^+ resonances observed in the pristine material). Since there are more Na^+ ions in the material at this state of charge than were present in the pristine material, Na^+ ions must intercalate into many more sites in the structure, with concurrent reduction of nearby Mn species. Hence, a broader distribution of Na^+ local environments is expected, which accounts for the broader distribution of chemical shifts in the ^{23}Na spectrum. In addition, the resonances seen at the end of discharge are broader and lower in intensity than at earlier stages of discharge, indicating slower Na^+ motion, as anticipated from the low concentration of Na^+ vacancies and higher concentration of Mn^{3+} ions (leading to slower Na^+ ion hopping) at this state of charge.

At the end of the second charge, the various ^{23}Na resonances appear at slightly higher Larmor frequencies than at the end of the first charge (approximately 1680 and 1270 ppm on second charge, compared to 1670 and 1260 ppm on first charge). This result reflects a change in the local bond angles and distances between Mn^{4+} and Na^+, presumably due to irreversible structural changes during the first charge–discharge cycle, but the intensities are significantly different. The low-shift feature has a higher intensity compared to the end of first charge, whilst the high-shift feature has a lower intensity. This suggests that more Na^+ ions are now trapped in the stacking-faulted layers compared to the first charge process, perhaps because the material now has more O-type layers. This is also consistent with the ^{7}Li NMR, where a wider distribution of low-shift (450 ppm) resonances was observed, suggesting more Li^+ ions in O-type layers (and therefore an increase in the number of O-type layers overall).

The spectrum at 4.1 V during the second discharge remains similar to the spectrum at 4.1 V on the first discharge, but with a lower signal intensity, which we assign to more infrequent Na^+ hopping (compared to first discharge).

2.5. Electronic Structure Evolution

We went on to investigate the charge compensation mechanism using XAS at the Mn L-edge and O K-edge and RIXS for O K-edge, performed at different states of charge (Figure S9b, Supporting Information). Oxy–20Li was used for this study as a representative example of this system. XAS for the Mn L-edge was measured using IPFY which provides bulk sensitive and nondistorted spectra.[40] **Figure 9**a,b shows collected spectra during the first charge and discharge, respectively, over the Mn L-edge. The spectrum of the pristine sample demonstrates the spectral fingerprints of Mn^{4+} with peaks at 640 and 644 eV in the L_3-edge. After charge to 4.1 V (CH 4.1 V), a shoulder feature corresponding to Mn^{3+} emerges (just below 640 eV); this persists in the middle of plateau (CH 4.22 V) and at the end of charge to 4.4 V (CH 4.4 V). Upon subsequent discharge to 4.1 V (DIS 4.1 V), the shoulder corresponding to Mn^{3+} disappears. A striking shift towards lower energy is found upon further discharge to 1.8 V (DIS 1.8 V).

At the O K-edge, O 1s core electrons are excited into unoccupied states above the Fermi level. Figure 9c exhibits the bulk sensitive PFY signals where the pre-edge region between 528.5 and 533.0 eV is associated with O 2p orbitals hybridized with Mn 3d orbitals. The intensity changes in the O 2p–Mn 3d hybridization agree well with those in Mn L-edge spectra; decreased intensity for CH 4.1 and progressively increased intensity for CH 4.22 and CH 4.4 V followed by a significant drop in intensity for DIS 1.8 V. Figure 9d illustrates the integrated intensity between 527 and 533 eV, relative to that of the pristine sample, corresponding to a measure of the changes in the density of hole states just above the Fermi level. When charging the material to 4.1 V, the intensity decreases consistent with the appearance of the Mn^{3+} feature in the Mn L-edge. This peculiar drop is also observed in P3-type $Na_{0.67}Ni_{0.2}Mn_{0.8}O_2$ in which oxygen oxidation occurs along with reduction of Ni, forming Ni 3d–O 2p hybridization.[41] It is also shown that the ligand-to-metal charge transfer is very strong when Mn is tetravalent in $LiMn_2O_4$, leading to a d^3L configuration rather than d^4.[42] The previous studies can be reconciled with our current observation, namely, reduction of Mn^{4+} occurs in the hybridized Mn 3d and O 2p states when the material is fully charged. Across the plateau, the increases in the hole density by 5% and 7% for CH 4.22 V and CH 4.4 V, respectively, can be explained by the removal of electrons from oxygen anions. Upon discharge to 4.1 V, a combination of the presence of Mn^{4+} and the reduction of oxygen anions results in a minor decrease in the density of hole states. The additional decrease in the integrated intensity for DIS 1.8 V originates from the high concentration of Mn^{3+}.

To obtain further insight into the nature of the O hole states, O K-edge RIXS spectra were collected on the oxy–20Li system during the first charge–discharge process. RIXS detects the emission from the O 2p valence states below the Fermi level and is therefore sensitive to changes in the electronic structure and oxidation states of oxygen. Figure 9e shows the O K-edge RIXS spectra centered at an emission energy of 525 eV for an excitation energy of 530.5 eV. A novel spectral feature at about 524 eV is observed as well as a slight shift of the main peak at 526 eV toward lower emission energy, implying the creation of a new set of electronic states arising from ligand-to-metal charge transfer (MLCT). The position of this novel sub-band shifts to higher energy for more highly charged samples (CH 4.22 V and CH 4.4 V), suggesting an

© 2021 The Authors. Advanced Energy Materials published by Wiley-VCH GmbH

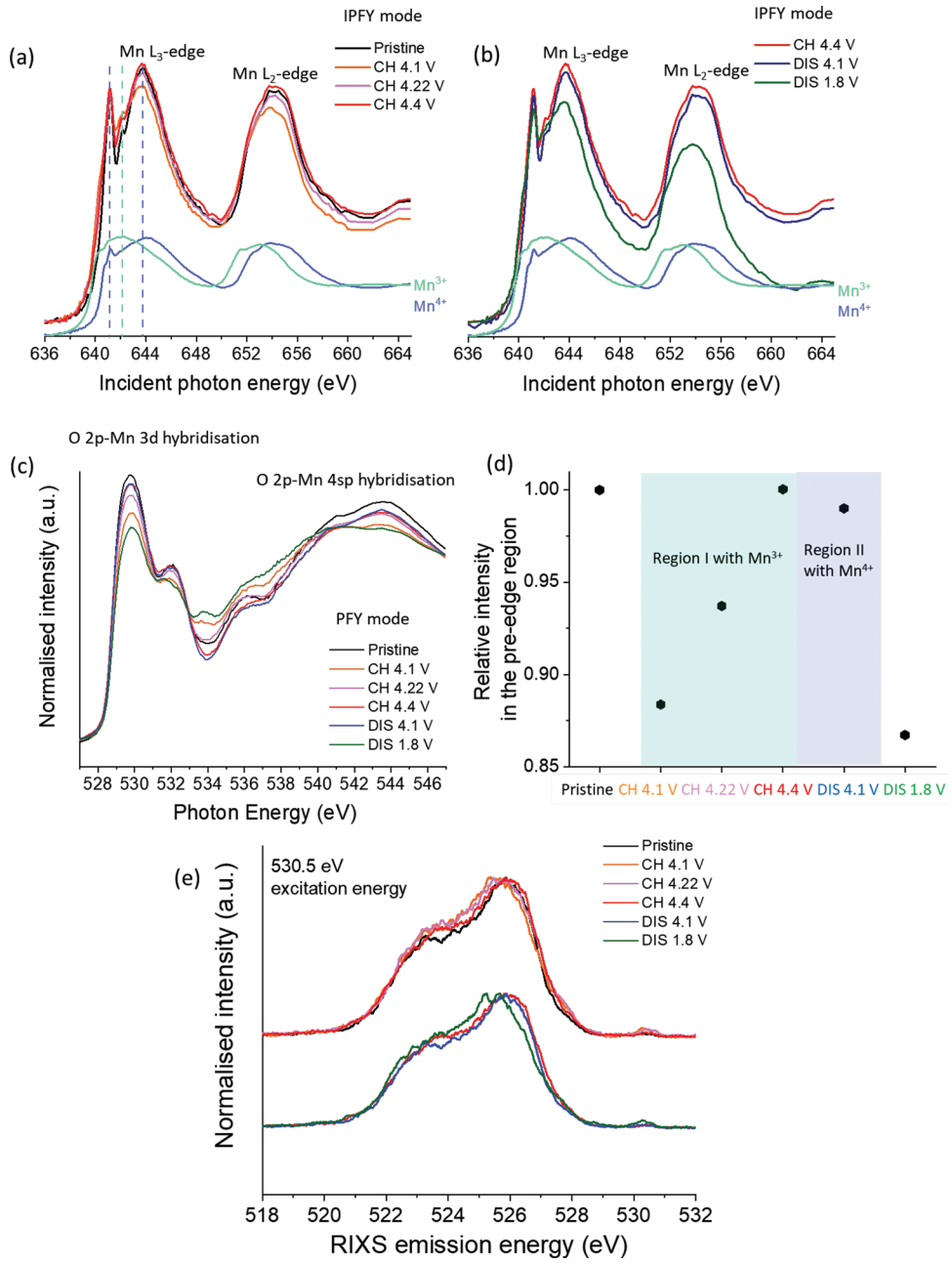

Figure 9. XAS for Mn L-edge measured at IPFY mode for a) as-prepared, charge to 4.1 V (orange), 4.22 V (magenta) and 4.4 V (red) b) charge to 4.4 V (red) and discharge to 4.1 V (blue) and 1.8 V (green) of oxy–20Li. c) XAS for O K-edge measured at PFY mode. d) Variation of the relative integrated intensity in the pre-edge region. e) RIXS spectra at an excitation energy of 530.5 eV.

increased number of oxygen holes created. Note that this is also corroborated by a strong increase in the low-energy RIXS region (despite its relatively small absolute intensity) just below the elastic scattering energy (530.5 eV), which indicates the emergence of a localized O-states without involving molecular oxygen.[12] The shift in energy is consistent with the electronic reshuffling process seen in oxygen-redox-active layered LIB cathodes.[17] The subsequent fading behavior of this peak correlates strongly with that of the MLCT feature. On discharging to 4.1 V (DIS 4.1 V), the electronic structure changes in both Mn 3d and O 2p result in complex spectra. Considering the reduced shoulder at around 524 eV, the new states seem to disappear, while the main peak shifts to lower energies at the end of discharge (DIS 1.8 V), corresponding to the formation of Mn^{3+}.

In summary, these spectroscopic studies of electronic structural changes indicate that strongly hybridized Mn 3d–O 2p orbitals favor ligand-to-metal charge transfer (a reductive coupling mechanism) facilitating reversible oxygen redox. This feature is emphasized in the P3-type material compared to the P2-type counterpart, probably originating from the maintained P3 structure in the high voltage

© 2021 The Authors. Advanced Energy Materials published by Wiley-VCH GmbH

region which can accommodate the strain induced by collective distortion.[43]

3. Conclusion

P3-type $Na_{0.67}Li_{0.2}Mn_{0.8}O_2$ is shown to adopt a ribbon superstructure in the transition metal layer analogous to that shown by P2 structure $Na_{0.6}Li_{0.2}Mn_{0.8}O_2$ reported by House et al.[12] The well-maintained ribbon superstructure with almost zero-strain during cycling and reversible Li migration in and out of the transition metal layers play essential roles in mitigating the large voltage hysteresis which plagues most oxygen-redox-active materials. In addition, the participation of oxygen anions in the charge compensation mechanism has been thoroughly investigated using ex situ SXAS and RIXS: oxidized O species were found to be stabilized through a reductive coupling mechanism, where rehybridization of the Mn 3d and O 2p states takes place during charge. We anticipate these processes are linked, with the migration of Li^+ ions facilitating and stabilizing the rehybridization process. By preparing the material under three different synthetic conditions the degree of cationic ordering may be varied to some extent. Increased cationic ordering tends to deliver increased capacity in both the wide voltage range of 1.6–4.4 V and over the narrower 3.5–4.3 V window where the capacity arises largely from anion redox.

4. Experimental Section

Stoichiometric amounts of sodium carbonate (Na_2CO_3, Fisher Chemistry, ≥99.5%) and lithium carbonate (Li_2CO_3, Fluka, ≥99.0%) were dissolved in deionized water (solution A). A separate aqueous solution of manganese (II) acetate tetrahydrate ($Mn(CH_3CO_2)_2{\cdot}4H_2O$, Sigma-Aldrich, ≥99%) was prepared (solution B). Solution A was added dropwise to solution B under stirring and then left to stir for a further 15 min. Water was removed using a rotary evaporator. The resulting solid was heated to 300 °C at a rate of 6 °C min^{-1} for 12 h and cooled to 50 °C at a rate of 6 °C min^{-1}. The powder was then ground and heated to 625 °C at a rate of 5 °C min^{-1} under different atmospheres for various dwell times and cooled at different cooling rates. The nomenclature of the samples is explained in **Table 4**. After synthesis, each pristine powder sample was stored in an Ar-filled glovebox to avoid degradation by atmospheric moisture.

Powder X-ray diffraction (PXRD) patterns of the as-synthesized compounds were recorded on a PANalytical Empyrean diffractometer in Bragg-Brentano geometry with Cu Kα_1 radiation ($\lambda = 1.5406$ Å). Samples were loaded in 0.5 mm glass capillaries and synchrotron powder X-ray diffraction data were obtained using the I11 diffractometer at the Diamond Light Source, UK (wavelength 0.826579(5) Å). Time-of-flight powder neutron diffraction (PND) data for the air–20Li material were obtained on the Polaris diffractometer at ISIS at the Rutherford Appleton Laboratory. The sample was contained in a 6 mm vanadium can. Structures were refined by the Rietveld method using Topas Academic v6.[44] Scanning electron microscopy (SEM) images of as-synthesized materials were recorded on either a JEOL JSM-5600 or JSM-6700F.

Table 4. Nomenclature of as-synthesized samples.

	Atmosphere	Heat treatment time	Cooling rate
Air–20Li	Air	3 h	Quench
Oxy–20Li	Oxygen	3 h	5 °C min^{-1}
Air–20Li–60 h	Air	60 h	5 °C min^{-1}

To evaluate the electrochemical performance of the materials, slurries were prepared using the active material, super C65 carbon, and Solef 5130 binder (a modified polyvinylidene fluoride (PVDF)) in mass ratios of 75:15:10 in *N*-methyl-2-pyrrolidone, which was then cast on aluminum foil using a doctor blade. After initial drying, 12 mm diameter electrode discs were punched then dried at 80 °C under vacuum for 12 h. CR2325 coin cells were assembled in an Ar-filled glovebox and used to evaluate the electrochemical performance. The cells consisted of a disc electrode, sodium metal as a counter/reference electrode, a glass fiber separator (Whatman, GF/F) and 1 M $NaClO_4$ in propylene carbonate containing 3% fluoroethylene carbonate by weight as the electrolyte. Galvanostatic charge/discharge cycling was carried out at 30 °C using a Maccor Series 4200 battery cycler or Biologic BCS-805 system.

In order to prepare electrochemically cycled samples for ex situ characterization, working electrodes were constructed by mixing the active material and super C65 carbon in mass ratios of 75:25 with no binder. The mixture was dried at 110 °C under vacuum for 12 h. For ex situ soft X-ray absorption spectroscopy (SXAS) and resonant inelastic X-ray scattering (RIXS), CR2325 coin cells were assembled as described above except that Solupor membranes replaced the glass fiber separator. For ex situ measurements for NMR and X-ray photoelectron spectroscopy (XPS) studies, Swagelok-type cells were assembled in an Ar-filled glovebox. The cells consisted of a desired amount of working electrode, sodium metal as a counter/reference electrode, glass fiber separators (Whatman, GF/F) and the electrolyte (1 M $NaClO_4$ in propylene carbonate containing 3% fluoroethylene carbonate by weight). For all ex situ measurements, cycled cells were transferred to an Ar-filled glovebox before opening and the active material was extracted. The electrodes were rinsed carefully with dry dimethyl carbonate to remove residual electrolyte and then left under vacuum for 12 h to ensure all solvent had evaporated. NMR, XPS, SXAS, and RIXS measurements on the cycled samples were carried out as described below.

All samples for ^{7}Li and ^{23}Na NMR experiments were packed into 1.3 mm diameter ZrO_2 magic angle spinning (MAS) rotors in an Ar-filled glovebox. ^{7}Li NMR spectra were referenced to solid Li_2CO_3 at 0 ppm, whilst ^{23}Na NMR spectra were referenced to solid NaCl at 7.21 ppm. NMR spectra were acquired on a Bruker Avance II (4.7 T) using a Bruker 1.3 mm MAS probe and MAS frequencies of 40 kHz for ^{7}Li NMR and 60 kHz for ^{23}Na NMR. A rotor-synchronized Hahn-echo pulse sequence (90°–τ–180°–τ–acquire) was used for quantitative measurements. $\frac{\pi}{2}$ pulse lengths of 1.04 µs and 0.58 µs for ^{7}Li and ^{23}Na, respectively, with recycle delays of 20 ms for both sets of spectra, such that the bulk, paramagnetically shifted signal was recorded quantitatively, while the diamagnetic signal (due to electrolyte decomposition products and/or surface impurities such as Li_2CO_3, LiOH, Na_2CO_3, and LiOH) was suppressed. Projection magic angle turning phase-adjusted sideband separation (pjMATPASS) experiments were also recorded to separate the isotropic resonances from the overlapping spinning sideband manifold.[31]

XPS measurements were carried out using a Kratos Ultra DLD (AXIS) instrument with a monochromatic aluminum K_α (1486.6 eV) X-ray source. All peaks were calibrated based on the hydrocarbon species C 1s peak at 285 eV. The spectra were analyzed using the CasaXPS software.

SXAS and RIXS experiments were performed at beamline BL27SU at Spring 8 in Japan.[45] Bulk-sensitive SXAS spectra were obtained in partial fluorescence yield (PFY) mode and inverse partial fluorescence yield (IPFY) mode, is the latter derived by inverting the O K-edge PFY. All SXAS spectra were normalized by the incident intensity, measured by recording the sample drain current and focusing the mirror current using pico-ammeters. Baselines were fitted to the mostly flat regions below any absorption peaks and subsequently subtracted from each spectrum. Further normalization was carried out by setting the low energy region before any absorption peaks to zero and the post-edge region after any absorption features to unity.

© 2021 The Authors. Advanced Energy Materials published by Wiley-VCH GmbH

In situ synchrotron XRD data were collected on the powder diffraction beamline at the Australian Synchrotron with a wavelength (λ) of 0.72725 Å. Data runs were 3.46 min, taken every 13.83 min on a coin cell in transmission geometry throughout the cycles. Full details of the experimental setup are provided elsewhere.[46] The coin cells were first charged to 4.4 V at 60 mA g^{-1} then discharged to 1.8 V at 30 mA g^{-1} and the second cycle was performed over the voltage window 1.8-4.4 V at 30 mA g^{-1}. The active material loading was 2.8 mg. Sequential Rietveld refinements were carried out using the GSAS-II program.[47]

Supporting Information

Supporting Information is available from the Wiley Online Library or from the author.

Acknowledgements

The authors are grateful for the provision of beam time and assistance from instrument scientists at beamlines I11 at Diamond (Rapid Access experiment CY26699), BL27SU at Spring8 and Powder Diffraction at the Australian Synchrotron (Australian Nuclear Science and Technology Organization). This work was supported by the Faraday Institution (grant number FIRG018) and the Australian Research Council (discovery and future fellowship programs DP170100269/DP200100959 and FT200100707). The authors thank Dr. H. Menard for his assistance with the XPS measurements. E.B. acknowledges funding from the Engineering Physical Sciences Research Council (EPSRC) via the National Productivity Interest Fund (NPIF) 2018 and is also grateful for use of the ARCHER UK National Supercomputing Service via our membership in the UK's HEC Materials Chemistry Consortium, funded by the EPSRC (EP/L000202). Research was also carried out at the Center for Functional Nanomaterials, Brookhaven National Laboratory, through the U.S. Department of Energy, Office of Basic Energy Sciences, Contract DE-AC02-98CH10866.

Conflict of Interest

The authors declare no conflict of interest.

Data Availability Statement

The data that support the findings of this study are available from the corresponding author upon reasonable request.

Keywords

layered structures, oxygen redox, P3 structure, sodium-ion batteries, superstructures

Received: July 30, 2021
Revised: November 22, 2021
Published online:

[1] N. Ortiz-Vitoriano, N. E. Drewett, E. Gonzalo, T. Rojo, *Energy Environ. Sci.* **2017**, *10*, 1051.
[2] R. J. Clément, P. G. Bruce, C. P. Grey, *J. Electrochem. Soc.* **2015**, *162*, A2589.
[3] C. Delmas, C. Fouassier, P. Hagenmuller, *Phys. B* **1980**, *99*, 81.
[4] K. Kubota, S. Kumakura, Y. Yoda, K. Kuroki, S. Komaba, *Adv. Energy Mater.* **2018**, *8*, 1703415.
[5] Y. You, A. Manthiram, *Adv. Energy Mater.* **2018**, *8*, 1701785.
[6] E. De La Llave, E. Talaie, E. Levi, P. K. Nayak, M. Dixit, P. T. Rao, P. Hartmann, F. Chesneau, D. T. Major, M. Greenstein, D. Aurbach, L. F. Nazar, *Chem. Mater.* **2016**, *28*, 9064.
[7] J. Billaud, G. Singh, A. R. Armstrong, E. Gonzalo, V. Roddatis, M. Armand, T. Rojo, P. G. Bruce, *Energy Environ. Sci.* **2014**, *7*, 1387.
[8] R. J. Clément, J. Billaud, A. R. Armstrong, G. Singh, T. Rojo, P. G. Bruce, C. P. Grey, *Energy Environ. Sci.* **2016**, *9*, 3240.
[9] S. Mariyappan, T. Marchandier, F. Rabuel, A. Iadecola, G. Rousse, A. V. Morozov, A. M. Abakumov, J. M. Tarascon, *Chem. Mater.* **2020**, *32*, 1657.
[10] K. Du, J. Zhu, G. Hu, H. Gao, Y. Li, J. B. Goodenough, *Energy Environ. Sci.* **2016**, *9*, 2575.
[11] X. Rong, J. Liu, E. Hu, Y. Liu, Y. Wang, J. Wu, X. Yu, K. Page, Y. S. Hu, W. Yang, H. Li, X. Q. Yang, L. Chen, X. Huang, *Joule* **2018**, *2*, 125.
[12] R. A. House, U. Maitra, M. A. Pérez-Osorio, J. G. Lozano, L. Jin, J. W. Somerville, L. C. Duda, A. Nag, A. Walters, K.-J. Zhou, M. R. Roberts, P. G. Bruce, *Nature* **2020**, *577*, 502.
[13] U. Maitra, R. A. House, J. W. Somerville, N. Tapia-Ruiz, J. G. Lozano, N. Guerrini, R. Hao, K. Luo, L. Jin, M. A. Pérez-Osorio, F. Massel, D. M. Pickup, S. Ramos, X. Lu, D. E. McNally, A. V. Chadwick, F. Giustino, T. Schmitt, L. C. Duda, M. R. Roberts, P. G. Bruce, *Nat. Chem.* **2018**, *10*, 288.
[14] B. Song, E. Hu, J. Liu, Y. Zhang, X. Q. Yang, J. Nanda, A. Huq, K. Page, *J. Mater. Chem. A* **2019**, *7*, 1491.
[15] X. Bai, M. Sathiya, B. Mendoza-Sánchez, A. Iadecola, J. Vergnet, R. Dedryvère, M. Saubanère, A. M. Abakumov, P. Rozier, J. M. Tarascon, *Adv. Energy Mater.* **2018**, *8*, 1802379.
[16] A. Konarov, J. H. Jo, J. U. Choi, Z. Bakenov, H. Yashiro, J. Kim, S. T. Myung, *Nano Energy* **2019**, *59*, 197.
[17] W. E. Gent, K. Lim, Y. Liang, Q. Li, T. Barnes, S. J. Ahn, K. H. Stone, M. McIntire, J. Hong, J. H. Song, Y. Li, A. Mehta, S. Ermon, T. Tyliszczak, D. Kilcoyne, D. Vine, J. H. Park, S. K. Doo, M. F. Toney, W. Yang, D. Prendergast, W. C. Chueh, *Nat. Commun.* **2017**, *8*, 2091.
[18] J. Vinckeviciute, D. A. Kitchaev, A. Van Der Ven, *Chem. Mater.* **2021**, *33*, 1625.
[19] B. Mortemard de Boisse, S. ichi Nishimura, E. Watanabe, L. Lander, A. Tsuchimoto, J. Kikkawa, E. Kobayashi, D. Asakura, M. Okubo, A. Yamada, *Adv. Energy Mater.* **2018**, *8*, 1800409.
[20] Y. Li, X. Wang, Y. Gao, Q. Zhang, G. Tan, Q. Kong, S. Bak, G. Lu, X.-Q. Yang, L. Gu, J. Lu, K. Amine, Z. Wang, L. Chen, *Adv. Energy Mater.* **2019**, *9*, 1803087.
[21] B. Song, M. Tang, E. Hu, O. J. Borkiewicz, K. M. Wiaderek, Y. Zhang, N. D. Phillip, X. Liu, Z. Shadike, C. Li, L. Song, Y. Y. Hu, M. Chi, G. M. Veith, X. Q. Yang, J. Liu, J. Nanda, K. Page, A. Huq, *Chem. Mater.* **2019**, *31*, 3756.
[22] D. A. Kitchaev, J. Vinckeviciute, A. van der Ven, *J. Am. Chem. Soc.* **2021**, *143*, 1908.
[23] C. Zhao, Q. Wang, Y. Lu, L. Jiang, L. Liu, X. Yu, L. Chen, B. Li, Y. S. Hu, *Energy Storage Mater.* **2019**, *20*, 395.
[24] X. Bai, A. Iadecola, J. Tarascon, P. Rozier, *Energy Storage Mater.* **2020**, *31*, 146.
[25] E. J. Kim, K. Mofredj, D. M. Pickup, A. V. Chadwick, J. T. S. Irvine, A. R. Armstrong, *J. Power Sources* **2020**, *481*, 229010.
[26] E. J. Kim, L. A. Ma, D. M. Pickup, A. V. Chadwick, R. Younesi, P. Maughan, J. T. S. Irvine, A. R. Armstrong, *ACS Appl. Energy Mater.* **2020**, *3*, 10423.
[27] Q. Wang, S. Mariyappan, G. Rousse, A. V. Morozov, B. Porcheron, R. Dedryvère, J. Wu, W. Yang, L. Zhang, M. Chakir, M. Avdeev, M. Deschamps, Y.-S. Yu, J. Cabana, M.-L. Doublet, A. M. Abakumov, J.-M. Tarascon, *Nat. Mater.* **2021**, *20*, 353.
[28] Y. S. Meng, G. Ceder, C. P. Grey, W. Yoon, M. Jiang, J. Bre, Y. Shao-Horn, *Chem. Mater.* **2005**, 17, 2386.

© 2021 The Authors. Advanced Energy Materials published by Wiley-VCH GmbH

[29] Z. Lu, Z. Chen, J. R. Dahn, *Chem. Mater.* **2003**, *15*, 3214.
[30] Z. Lu, L. Y. Beaulieu, R. A. Donaberger, C. L. Thomas, J. R. Dahn, *J. Electrochem. Soc.* **2002**, *149*, A778.
[31] I. Hung, L. Zhou, F. Pourpoint, C. P. Grey, Z. Gan, *J. Am. Chem. Soc.* **2012**, *134*, 1898.
[32] R. A. House, U. Maitra, L. Jin, J. G. Lozano, J. W. Somerville, N. H. Rees, A. J. Naylor, L. C. Duda, F. Massel, A. V. Chadwick, S. Ramos, D. M. Pickup, D. E. McNally, X. Lu, T. Schmitt, M. R. Roberts, P. G. Bruce, *Chem. Mater.* **2019**, *31*, 3293.
[33] J. Bréger, M. Jiang, N. Dupré, Y. S. Meng, Y. Shao-Horn, G. Ceder, C. P. Grey, *J. Solid State Chem.* **2005**, *178*, 2575.
[34] F. Dogan, J. R. Croy, M. Balasubramanian, M. D. Slater, H. Iddir, C. S. Johnson, J. T. Vaughey, B. Key, *J. Electrochem. Soc.* **2015**, *162*, A235.
[35] X. Rong, E. Hu, Y. Lu, F. Meng, C. Zhao, X. Wang, Q. Zhang, X. Yu, L. Gu, Y. S. Hu, H. Li, X. Huang, X. Q. Yang, C. Delmas, L. Chen, *Joule* **2019**, *3*, 503.
[36] G. Assat, J. M. Tarascon, *Nat. Energy* **2018**, *3*, 373.
[37] Y. H. Jung, A. S. Christiansen, R. E. Johnsen, P. Norby, D. K. Kim, *Adv. Funct. Mater.* **2015**, *25*, 3227.
[38] J. Xu, D. H. Lee, R. J. Clément, X. Yu, M. Leskes, A. J. Pell, G. Pintacuda, X.-Q. Yang, C. P. Grey, Y. S. Meng, *Chem. Mater.* **2014**, *26*, 1260.
[39] K. Märker, P. J. Reeves, C. Xu, K. J. Griffith, C. P. Grey, *Chem. Mater.* **2019**, *31*, 2545.
[40] D. Asakura, E. Hosono, Y. Nanba, H. Zhou, J. Okabayashi, C. Ban, P. A. Glans, J. Guo, T. Mizokawa, G. Chen, A. J. Achkar, D. G. Hawthron, T. Z. Regier, H. Wadati, *AIP Adv.* **2016**, *6*, 035105.
[41] E. J. Kim, L. A. Ma, L. C. Duda, D. M. Pickup, A. V. Chadwick, R. Younesi, J. T. S. Irvine, A. R. Armstrong, *ACS Appl. Energy Mater.* **2020**, *3*, 184.
[42] D. Asakura, Y. Nanba, E. Hosono, M. Okubo, H. Niwa, H. Kiuchi, J. Miyawaki, Y. Harada, *Phys. Chem. Chem. Phys.* **2019**, *21*, 18363.
[43] J. Vergnet, M. Saubanere, M. Doublet, J. M. Tarascon, *Joule* **2020**, *4*, 420.
[44] A. A. Coelho, *J. Appl. Crystallogr.* **2000**, *33*, 899.
[45] Y. Tamenori, H. Ohashi, E. Ishiguro, T. Ishikawa, *Rev. Sci. Instrum.* **2002**, *73*, 1588.
[46] N. Sharma, N. Tapia-Ruiz, G. Singh, A. R. Armstrong, J. C. Pramudita, H. E. A. Brand, J. Billaud, P. G. Bruce, T. Rojo, *Chem. Mater.* **2015**, *27*, 6976.
[47] B. H. Toby, R. B. Von Dreele, *J. Appl. Crystallogr.* **2013**, *46*, 544.

© 2021 The Authors. Advanced Energy Materials published by Wiley-VCH GmbH